Metals and Materials International, Available online 21 September 2024
DOI: 10.1007/s12540-024-01797-4

Compressive properties and fracture behaviours of Ti/Al interpenetrating phase composites with additive-manufactured triply periodic minimal surface porous structures

Zhou Li[1, 2], *Haotian* Mo[1, 2], *Jiahao* Tian[1, 2], *Junhao* Li[1, 2], *Shiqi* Xia[1, 2*], *Xianshi* Jia[1, 2*], *Libo* Zhou[3], and *Yao* Lu[4]

[1] College of Mechanical and Electrical Engineering, Central South University, Changsha 410083, China

[2] State Key Laboratory of Precision Manufacturing for Extreme Service Performance, Changsha 410083, China

[3] School of Energy and Power Engineering, Changsha University of Science & Technology, Changsha 410114, China

[4] Welding and Additive Manufacturing Centre, Cranfield University, Bedfordshire, MK43 0AL, UK

Abstract

The triply periodic minimal surfaces (TPMS) structure is regarded as a highly promising artificial design, but the performance of composites constructed using this structure remains unexplored. Two porosity levels of Ti/Al interpenetrating phase composites (IPCs) were fabricated by infiltrating ZL102-Al melt into additive-manufactured TC4-Ti scaffolds with the TPMS porous in this study. The combination of the two-phase alloys exhibits structural integrity at the interfacial region, as evidenced by microscopic surfaces observed in uncompressed IPCs. Quasi-static compression tests were performed to demonstrate that the Young's modulus, yield stress and maximum compressive stress of IPCs exhibit significant enhancement when compared to the individual TPMS scaffolds, due to the supporting and strengthening effect of the filling phase. In the compression process of IPCs, defects emerge initially at the interface between the ZL102 phase and TC4 phase, triggering the fracture and slip of the ZL102 phase, eventually propagating to involve fracture in the TC4 phase. The deformation behaviours obtained from numerical simulation were combined to support these experimental phenomena. The results show that the corresponding stress concentration region is the central region of the spiral surface, the maximum stress concentration region of the ZL102 phase is the same as that of the TC4 phase, and the ZL102 phase effectively shares part of the loading. The Ti/Al IPCs achieve equivalent load-bearing capacity through a simplified interpenetration process and the utilisation of lighter materials.

Keywords: Additive manufacturing; Triply periodic minimal surface; Interpenetrating phase composites; Porous structure; Compressive properties

* Corresponding author: shiqixia@csu.edu.cn, 221026@csu.edu.cn

Published by Springer. This is the Author Accepted Manuscript issued with: Creative Commons Attribution License (CC:BY 4.0).
The final published version (version of record) is available online at DOI:10.1007/s12540-024-01797-4. Please refer to any applicable publisher terms of use.

1 Introduction

Metal composite materials achieve enhanced properties through the collaborative synergy of their constituent materials to meet the rigorous demands of modern industries [1, 2]. In traditional metal composites, a single metal serves as the matrix responsible for load-bearing, possessing rigidity and strength, while other materials contribute to load transmission. Solely the matrix can achieve a continuous state, lacking the ability for other metal materials to establish a topologically interconnected state, thereby imposing constraints on the concentration and internal connectivity of the composite matrix [3, 4]. These limits highlight the appeal of interpenetrating phase composites (IPCs), ensuring topological interconnection between the two phases throughout their microstructure [5-9]. This could help retain excellent characteristics of the required single material and overcome one or several performance defects of conventional metal composite, contributing to the development of excellent mechanical properties [10-16]. For instance, Mg/Ti IPCs exhibit an optimum combination of mechanical properties, including strength, elongation to fracture, work of fracture, and fracture and impact toughness [17]; TiC/Fe IPCs demonstrate enhanced hardness, toughness and structural integrity compared to the single constituent metal [18]; Al/Ti IPCs have excellent mechanical properties in metal composites while adhering to the lightweight design objective, and these IPCs deserve further research [19].

Manufacturing IPCs with controlled and complex topologies is being superior realised in the rapid development of metal additive manufacturing (MAM) [20-23], which offers unrivalled design freedom with the ability to manufacture different metal materials into hollow structures [24-26], porous structures [27-29], grid structures [30-33] and gradient functional structures [34-36]. According to the printing materials and various processing methods, MAM can be classified into many various types, such as selective laser melting (SLM) [37, 38], selective laser sintering (SLS) [39, 40], and electron beam melting (EBM) [41, 42]. In these techniques, focused lasers or electron beams are used to selectively sinter thin layers of metal powder particles that are evenly distributed on flat build plates, where another thin metal powder layer is bonded to the previously deposited metal on top of the already laid powder layer. Researchers and the industry exhibit heightened interest in the SLM technologies, where powders are melted to achieve sufficient surface diffusion of the particles, producing low-density green parts typically with inherent porosity and anisotropic mechanical properties, and some experimental results have found that triply periodic minimal surfaces (TPMS)-based IPCs have better mechanical properties [43].

TPMS structures present continuous and smooth infinite periodic surface in three independent directions, featuring a special spatial structure with two disjoint regions in space. These structures that possess numerous exceptional characteristics, encompassing light weight properties [44], excellent energy absorption effect, mechanical property [45], self-supporting characteristics, design flexibility and elimination of stress concentration effect [46], are widely used as structural forms of Diamond [47], Gyroid [48], IWP [49] and Primitive [50]. Colin Bonatti and Dirk Mohr [51] applied the TPMS structures to energy absorption devices, and Jia et al. [52] played the role of these porous structures in the lightweight design. Novak et al. [53] obtained the mechanical properties and energy absorption effects of these TPMS structures through quasi-static compression experiments and dynamic impact experiments, and concluded that Diamond and Gyroid structures have higher mechanical properties and energy absorption effects. Zahid Ahmed Qureshi et al. [54] studied the energy transfer performance of TPMS structures (Primitive, Gyroid and IWP) at three distinct levels of porosity: 60 %, 75 % and 90 %, and they proposed that the porosity of TPMS has a great influence on their performance.

Despite the extensive research efforts dedicated to exploring the mechanical properties of TPMS structures, the quest for a novel composite structure that effectively balances high performance and reduced weight remains ongoing. In pursuit of this objective, this work employed the well-established SLM additive manufacturing technology to fabricate a Ti substrate featuring TPMS as its basic scaffold, and the Al was utilised as the light alloy to form the IPCs using a gravity casting performed within an ultrasonic field environment. To cater to customised porosity needs, two kinds of Gyroid homogeneous TPMS structures were chosen, prepared, and then comparatively analysed in this study for their mechanical properties, microstructure, and compressive resistance in the newly fabricated Ti/Al IPCs. The investigation of this work is to provide a reference for the optimisation of the practical fabrication processing of metal composite materials.

2 Experimental procedures

2.1 Design and fabrication of composites

Commencing from mathematics, the minimal surface equation can be formulated by the level set approximation equation method [55]. The equation composed of trigonometric functions obtained by this method can be used to obtain a minimal periodic surface in three-dimensional space. The following are the mathematical governing equations for the chosen Gyroid cell:

$$-t \le \sin\left(\frac{2\pi}{a}\cdot x\right)\cos\left(\frac{2\pi}{a}\cdot y\right)+\sin\left(\frac{2\pi}{a}\cdot y\right)\cos\left(\frac{2\pi}{a}\cdot z\right)+\sin\left(\frac{2\pi}{a}\cdot z\right)\cos\left(\frac{2\pi}{a}\cdot x\right)\le t \qquad (1)$$

$$\begin{cases} \frac{\partial G}{\partial x}=\frac{2\pi}{a}\cos\left(\frac{2\pi}{a}\cdot x\right)\cos\left(\frac{2\pi}{a}\cdot y\right)-\frac{2\pi}{a}\sin\left(\frac{2\pi}{a}\cdot x\right)\sin\left(\frac{2\pi}{a}\cdot z\right) \\ \frac{\partial G}{\partial y}=\frac{2\pi}{a}\cos\left(\frac{2\pi}{a}\cdot y\right)\cos\left(\frac{2\pi}{a}\cdot z\right)-\frac{2\pi}{a}\sin\left(\frac{2\pi}{a}\cdot y\right)\sin\left(\frac{2\pi}{a}\cdot x\right) \\ \frac{\partial G}{\partial z}=\frac{2\pi}{a}\cos\left(\frac{2\pi}{a}\cdot z\right)\cos\left(\frac{2\pi}{a}\cdot x\right)-\frac{2\pi}{a}\sin\left(\frac{2\pi}{a}\cdot z\right)\sin\left(\frac{2\pi}{a}\cdot y\right) \end{cases} \quad (2)$$

where, a is the cell length, which controls the size of a single cell, t controls the volume fraction of the two regions divided by the surface of the gyroid structure. Note that when t=0, the volumes of these two regions are equal. The equation for the partial derivative function, as presented in Eq. (2), is derived from the implicit function of the Gyroid, expressed as G (x, y, z) in Eq. (1). The parameter, t, controls the wall thickness, influencing both the volume fraction of the pore phase (denoted as v^*) and the porosity of the solid phase (denoted as Φ). Eq. (3) represents the mathematical formula used to calculate the porosity [56]:

$$\Phi=\left(1-v^*\right)\cdot 100\ [\%] \quad (3)$$

Here the assignment value of a is set as 10, and the two assignment values of t are set as 0.3 and 0.5, respectively. Such setting of parameter values achieves the TPMS structure of two porosities, measuring 88.92 % and 67.19 %, respectively. Mathematical modeling was conducted to model and offset the Gyroid structure, ensuring surface accuracy, and the resulting 3D stereo-lithography (STL) model is imported for further analysis. The filling specification of the model is the size of 10 mm-sized cells, constituting a total of 5 layers. Each layer is composed of 4 evenly distributed cells, eventually forming a rectangular sample measuring 20×20×50 mm.

After the established model is adjusted to the stereolithographic format, the sample model is additive-manufactured by the FS121M-D printer with SLM as the printing method with a two-way powder laying system. The print size ranges from 15 to 53 μm, and the chemical composition of the powder is shown in Table 1. Its main component is TC4, known for its favorable comprehensive properties and structural stability. This alloy exhibits excellent toughness, plasticity and high-temperature deformation properties, making it well-suited for the thermal pressure processing. Additionally, it can undergo processing, such as quenching and aging to strengthen its alloy strength. The compressive specimens were made in the horizontal direction relative to the construction plate, and the construction plate is a molding bar with a size of 120×120×100 mm. The optimised process parameters were adopted: powder layer thickness of 30 μm, laser power of 200 W, laser spot diameter of 110 μm defocusing state, 68 μm focusing state, and scanning speed of 1100 mm/s. All the lattice specimens were constructed in the alternate scanning mode. At the same time, in order to keep the oxygen level

in the construction chamber below 0.1 %, ultra-high purity argon was injected into the construction chamber during the manufacturing process, and the construction plate was selected as an unheated substrate at normal temperature. The printed TC4 sample was heated rapidly to 800 ℃ under the condition of argon protection for heat treatment, held for 2 hours, and cooled together with the heating furnace.

During the casting process, an Al alloy (denoted as ZL102) was chosen, and its chemical composition is shown in Table 2, showcasing its excellent casting characteristics. The ZL102 was heated to 720 ℃ in the graphite crucible at a high pouring temperature to increase the fluidity of the molten alloy. The macroscopic structure of the casting is usually composed of cold crystal region, columnar crystal region and internal equiaxed crystal region, weakening the mechanical properties of materials. Therefore, the interference of ultrasonic field was selected to reduce the grain structure, thereby improving the corrosion resistance, strength and toughness of the casting [57, 58]. The graphite can was put into an industrial ultrasonic cleaning machine, adjusting the power to 120 W. Ultimately, the molten ZL102 was immediately poured into the graphite tank, penetrating into the cavity of the printed TPMS porous structure of TC4 alloy to fabricate the IPCs material under vacuum conditions. Following the cooling, the sample surface was polished with 800 mesh sandpaper for further mechanical testing. Fig. 1 shows the schematic diagram of the preparation of Ti/Al IPCs.

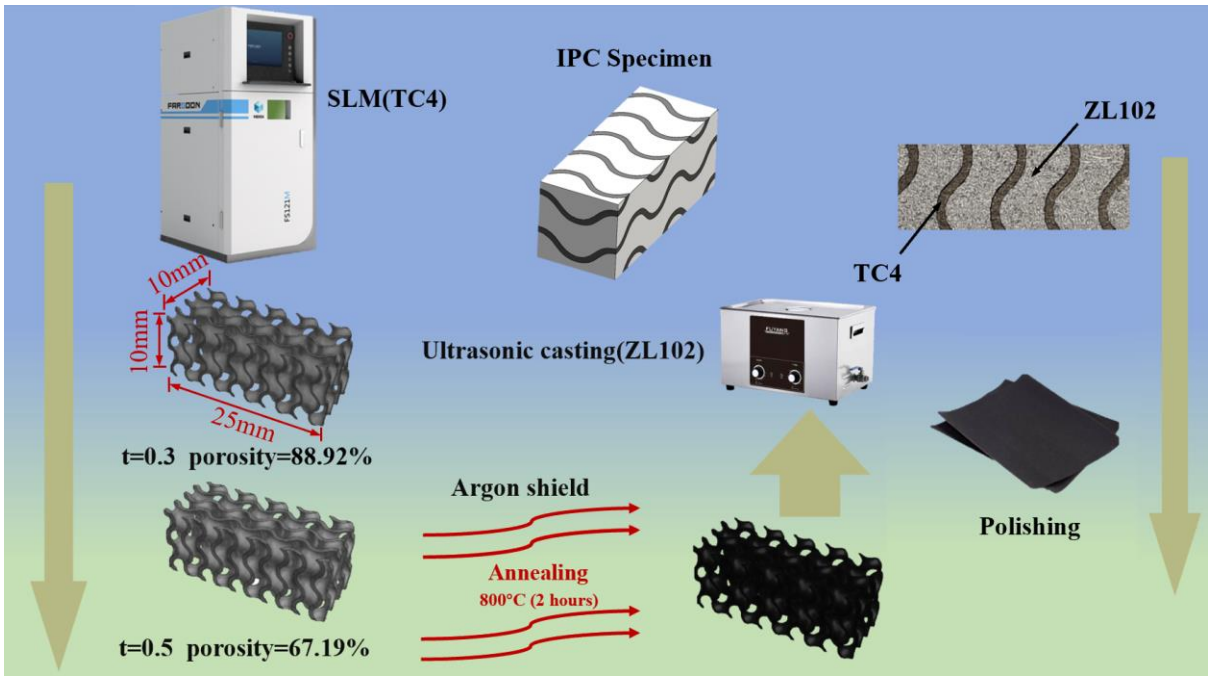

Fig. 1 Flowchart of preparation of Ti/Al IPCs with TPMS porous structures.

Table 1 Chemical composition of TC4 powder used as the feedstock material for SLM (wt. %).

Al	V	Fe	C	O	N	Y	Ti
5.70	3.63	0.13	0.0015	0.11	0.0036	0.0013	Balance

Table 2 Chemical composition of the ZL102 used for casting (wt. %).

Si	Fe	Cu	Mn	Mg	Ti	Zn	Al
10.0-13.0	<1.0	<0.3	<0.5	<0.1	<0.2	<0.3	Balance

2.2 Compressive testing, measurements and simulation method

All mechanical tests were performed on an Instron 8800 mechanical test frame equipped with a 100 KN loading force sensor, as shown in Fig. 2. All specimens were cut to 10×10×25 mm for the compression with a loading speed of 2 mm/min in all tests. The experiment involved replicating the TPMS structures, each with two distinct porosities, along with their corresponding IPCs, three times. After the compression testing, experimental specimens were cut from the IPCs. The optical microstructure of composite was investigated by the Nickon Eclipse LV100NDA optical microscope. A JSM-6490F scanning electron microscope (SEM) was utilised to scrutinize the morphology of the interfacial zone, and the distribution of elements was measured by energy-dispersive X-ray spectroscopy (EDS) using a spectrometer. Interphase constitutions were determined by micro-zone X-ray diffraction (XRD) using an X-ray micro-diffractometer radiation operating at power of 9 kW, scanning range of 10° to 80°and scanning speed of 5°/min. CAD models for IPCs and the TPMS lattices were utilised to perform finite element simulations in ABAQUS. These simulations aimed to scrutinise the deformations and stress distributions during quasi-static compressive loading. The external dimensions of the models were consistent with those employed in mechanical testing. For meshing, all models were divided using tetrahedral elements set at a size of 0.5 mm.

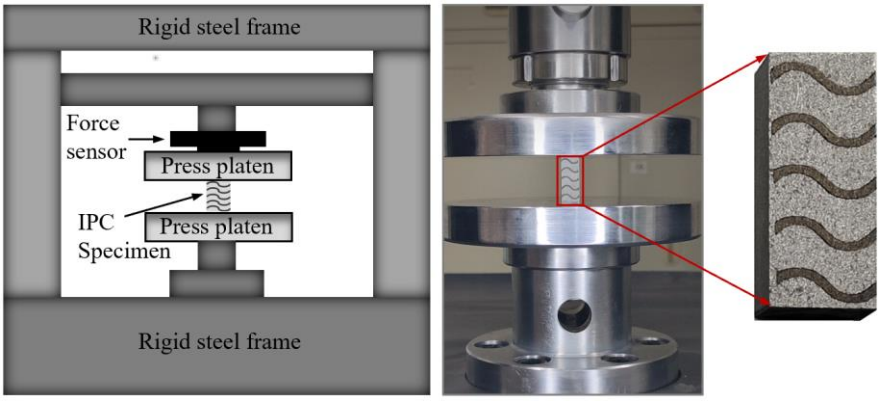

Fig. 2 Schematic diagram of compressive testing and the compression setup.

3 Results

3.1 Microstructural characterisation

Surface morphologies of printed TC4 scaffolds are presented in Fig. 3. No macro defects (cracks, pores and deformation) were observed due to the optimised parameters, indicating a favorable manufacturability of the TPMS structures. The SLM technique with horizontally-laying walls generated a visibly rough surface on the TC4 sample (Figs. 3a and 3b) [59]. However, the end face's material edge appears slightly flattened (Figs. 3c and 3d), suggesting that the edge area is more difficult to produce shrinkage defects and less likely to appear stress concentration after subsequent casting.

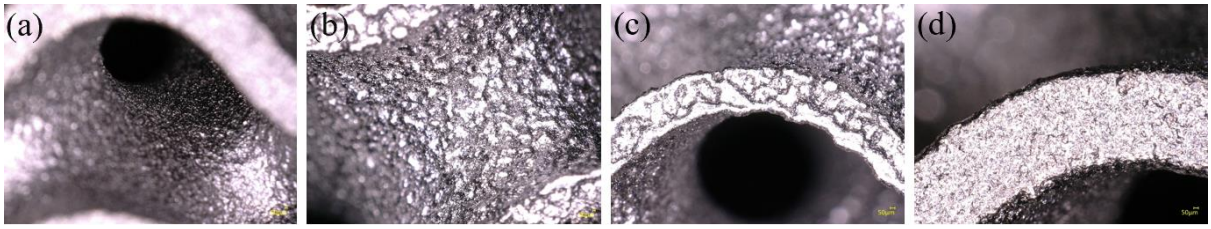

Fig. 3 Surface morpholoies of printed TC4 samples: (a-b) inside surface regions, and (c-d) marginal regions.

Microscopic surfaces of the uncompressed IPCs at the interfacial region and magnified views are shown in Fig. 4. It is noting that the combination of the two-phase alloys is sound, with a few minor defects visible at the interfacial region (Fig. 4b). This is due to the complex lattice structure in the casting space during the casting process. The amount of dissolved gas in the melt continue to rise, providing the basic conditions for the formation of these voids. In addition, the thermal conductivity of ZL102 is much higher than that of TC4, and the difference in thermal conductivity is more than 10 times, which makes the cooling speed of ZL102 much faster than that of TC4, resulting in residual stress at the interface and forming small defects. Through SEM microphotography of the interior of the two phases of the interpenetrating material, it can be seen that the surface of TC4 is smooth (Figs. 4e and 4f), while the surface of ZL102 has many irregular bumps and dents (Figs. 4c and 4d). The surface pellets of TC4 are caused by sintering defects, that is, not all metal powders can be effectively sintered. In addition, as a result of rapid cooling, layered fractures similar to rock formations form (Fig. 4e).

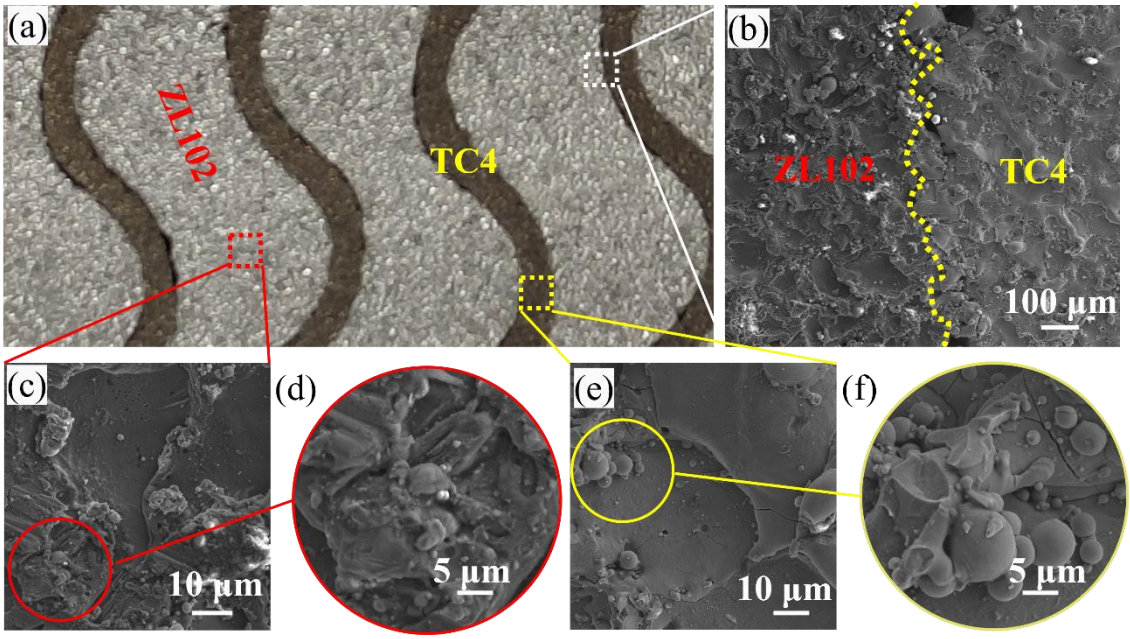

Fig. 4 Uncompressed microscopic images of TC4/ZL102 IPCs at the interfacial region and magnified views: (a) selected shooting position on TC4/ZL102 IPCs, (b) interfacial area between ZL102 and TC4 phases, (c) ZL102 phase structure, (d) a highly magnified image of (c), (e) TC4 phase structure, and (f) a highly magnified image of (e).

Fig. 5 shows the EDS mapping and XRD results of fabricated Ti/Al IPC in the interfacial zone. The uniform distribution of Ti and V elements in the TC4 grain boundary demonstrates a significant advantage of additive manufacturing compared to casting, namely the uniform distribution of alloying elements. Conversely, the limited accumulation of Mg element in ZL102 grain boundary is observed. This behaviour is attributed to the strengthening mechanism of ZL102 by the alloy element Mg, which discourages its accumulation in the ZL102 grain boundary. The element mapping between the ZL102 and TC4 phases indicates that no obvious diffusion of primary elements Al and Mg from ZL102, and Ti and V from TC4 occur between their respective region, but the surface of the printed TC4 scaffold is relatively rough resulting in ZL102 embedded in the TC4 scaffold to a certain extent (Figs. 5a and 5c). The XRD analysis confirms that no new intermediate compounds are formed adjacent to the interfacial zone (Fig. 5b). This is due to the fact that the printed TC4 scaffold has been heat-treated prior to casting and the fact that the formation of intermetallic compounds at the Ti/Al interface requires a high degree of temperature, structure, chemical composition and contact properties between the two phases. This similar phenomenon was reported that Ti64-AlSi9Cu3 IPCs based on cubic framework failed to reveal new metal compounds in the interfacial region [60].

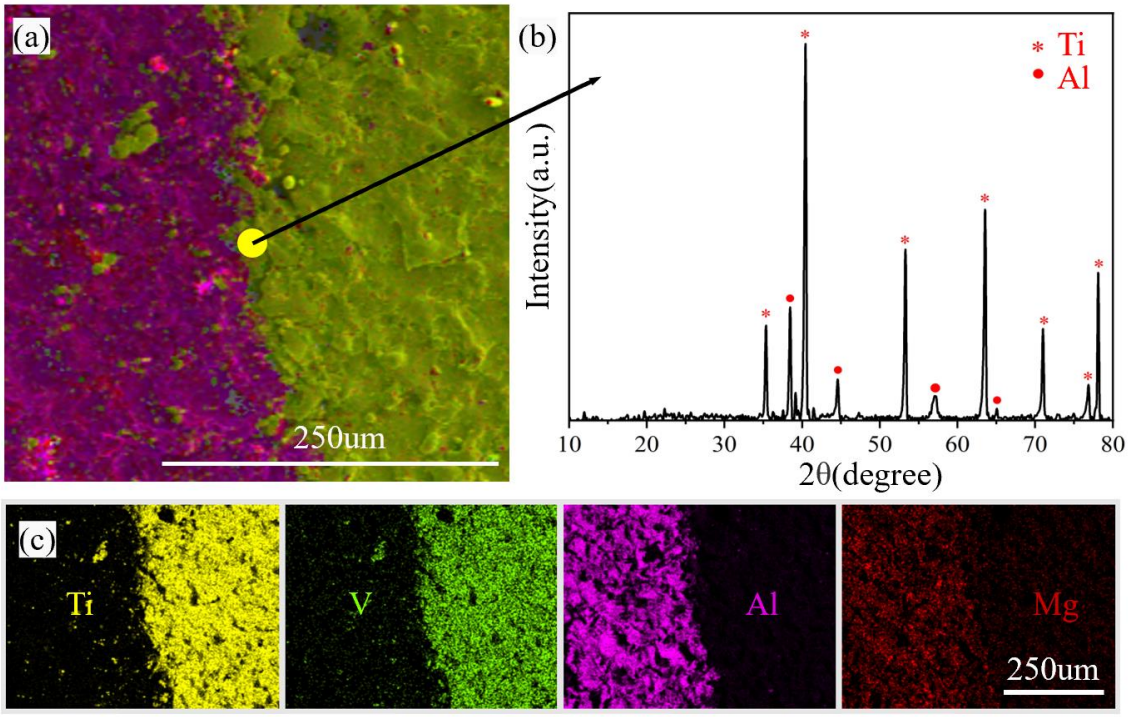

Fig. 5 (a) EDS mapping of the interface region between ZL102 and TC4 phases, (b) the XRD pattern at the interface, and (c) the elemental distributions of Ti, V, Al and Mg in the region corresponding to the image (a).

3.2 Quasi-static compressive properties

To explore the compressive properties of IPCs specimens, Fig. 6 shows the quasi-static compressive stress-strain curves of the TPMS scaffolds and the IPCs under two different porosities. The variation in porosity significantly affects the compression performance of the specimen. The flow stress of the TPMS scaffold with a lower porosity (67.19 % at t=0.5), approximately reaching 150 Mpa, is nearly double that of the TPMS scaffold with a higher porosity (88.92 % at t=0.3). In comparison to the individual TPMS scaffolds with both porosities, the IPCs exhibit superior compressibility, and relatively greater strength prior to specimen fracture. The IPC featuring a lower porosity TPMS structure (t=0.5) demonstrates a greater maximum compressive stress, reaching approximately 420 Mpa, compared to the IPC with a higher porosity TPMS structure (t=0.3). This improvement is attributed to the synergistic enhancement of each component achieved through interpenetrating phases [19]. From the perspective of composites, the addition of ZL102 phase also promoted the improvement of specimen compression performance.

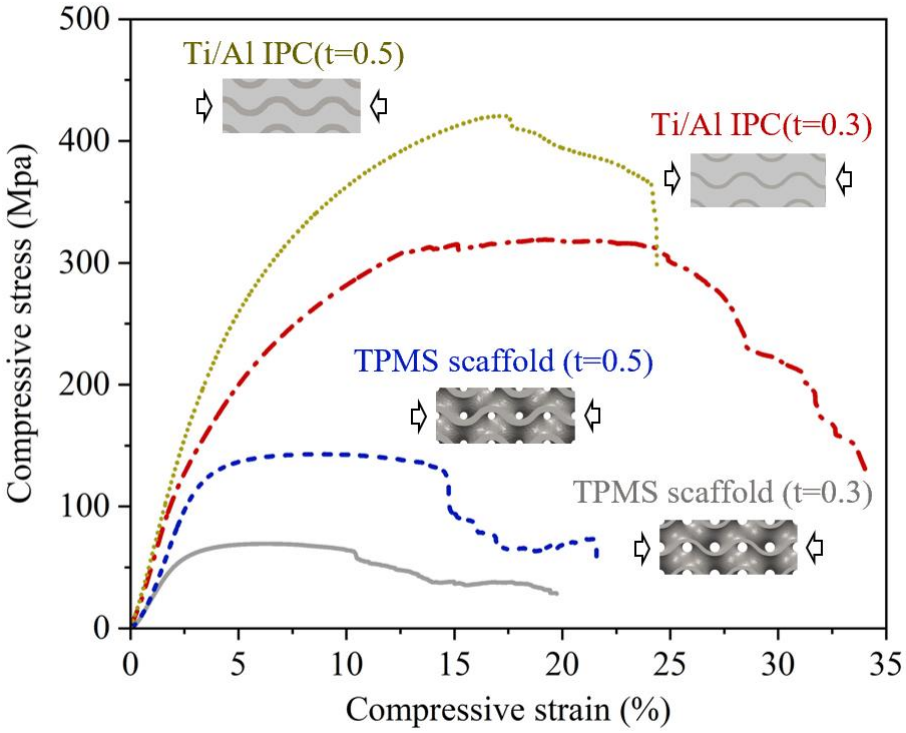

Fig. 6 The quasi-static compressive stress-strain curves of the TPMS scaffold and IPCs specimens under two different porosities of 0.3 and 0.5, respectively.

Table 3 shows other compression properties obtained in the compressive testing, including Young's modulus, the yield stress at the offset strain of 0.2 %, maximum compressive stress, reduction of compression to rupture, and work hardening coefficient (determined from the stress-strain curves of compression). The results reveal that although the reduction in deformation is relatively minor, the IPCs significantly enhance all five compressive properties, especially the maximum compressive stress. Even in the case of IPCs (t=0.3) is 4.6 times greater than that of the same porosity TPMS scaffold. Both the TPMS structure and the IPC with lower porosity (t=0.5) demonstrate yield stress, Young's modulus and maximum compressive stress 1.3-2.1 times higher compared to structures with a higher porosity, but these specimens with higher porosity have a higher work hardening coefficient. This reflects the more favourable strain hardening of the material as it continues to deform after it starts to yield. As the strain increases, the material aligns in the same direction, causing the localisation of the hardening coefficient to become more challenging. This results in higher strain peaks, compressibility and more uniform strain distribution for IPCs with high porosity TPMS structures, leading to more uniform deformation. The demonstrated outstanding mechanical properties and differences of IPCs underscore the effective contribution of interpenetrating structures in enhancing strength and compressibility. Meanwhile, the porosity level of the

interpenetrating structure in the composite has varying effects on enhancing the compressive stress limit and strain limit of the IPC.

Table 3 The compressive properties of each specimen.

Material	Yield stress (Mpa)	Young's modulus (Gpa)	Maximum compressive stress (Mpa)	Reduction (%)	Work hardening coeffcient
TPMS scaffold (t=0.3)	67 ± 2.5	28 ± 0.1	69 ± 2.5	19 ± 0.8	0.15 ± 0.05
IPC with a TPMS structure (t=0.3)	220 ± 2.0	56 ± 0.3	319 ± 5.5	34 ± 0.5	0.45 ± 0.02
TPMS scaffold (t=0.5)	138 ± 1.1	41 ± 0.8	142 ± 2.2	21 ± 0.5	0.12 ± 0.02
IPC with a TPMS structure (t=0.5)	305 ± 2.2	64 ± 0.1	420 ± 4.7	24 ± 0.8	0.42 ± 0.03

To enhance the analysis of the compression behaviour of Ti/Al IPCs, both numerical simulations and experiments are employed in combination. The compressive stress distributions of TPMS scaffolds and fracture areas of IPCs with two porosities obtained from the numerical simulations and compression experiments at the moment of initial cracking, respectively, are shown in Figs. 7a and 7c. The area enclosed by the box indicates the position of the initial stress concentration within the interpenetrating TPMS structure during the simulation, occurring at strain levels of 15 % for IPC with a TPMS structure (t=0.3) and 17 % for IPC with a TPMS structure (t=0.5). In the compression experiments, the IPCs also show severe cracking in the same regions under the approximate strain conditions. Combining the results of the compression tests in Fig. 6, it can be found that the flow stress of IPC with a TPMS structure (t=0.3) and IPC with a TPMS structure (t=0.5) show an initial significant change at the strains of around 15 % and 17 %, respectively. The former scenario occurs at 15% strain, where the flow stress of IPC gradually decreases, whereas the latter unfolds at 17% strain, with the flow stress of IPC entering a relatively constant platform. These verify that the interpenetrating TPMS structures suffer substantial stress damage, resulting in the initiation of cracking. It is worth noting that the stresses of IPCs reach their peak at the strain corresponding to the initiation of cracks in the interpenetrating structures. The emergence of cracks in the TPMS structure destroys the integrity and continuity of the Ti/Al IPC interpenetrated structure, leading to the degradation in the material's mechanical properties, and a similar phenomenon was observed in the structural analyses of Mg-NiTi IPC [6]. Additionally, from the beginning

of compression to the appearance of initial cracks, the numerical and experimental compressive stress-strain curves corresponding to the strain are shown in Figs. 7b and 7d. When the interpenetrating TPMS structure has an initial crack, the deviation of the two flow stresses is 5.4 % for IPC (t=0.3) and 6 % for IPC (t=0.5), respectively. The trends of the two curves are basically the same, but the actual experimental stresses are lower than the numerical results. It is crucial to acknowledge that the numerical simulation involves the direct allocation of material properties to the TPMS structure, but the TPMS structure utilised in the practical experiment is fabricated by the additive manufacturing, introducing a certain gap in performance.

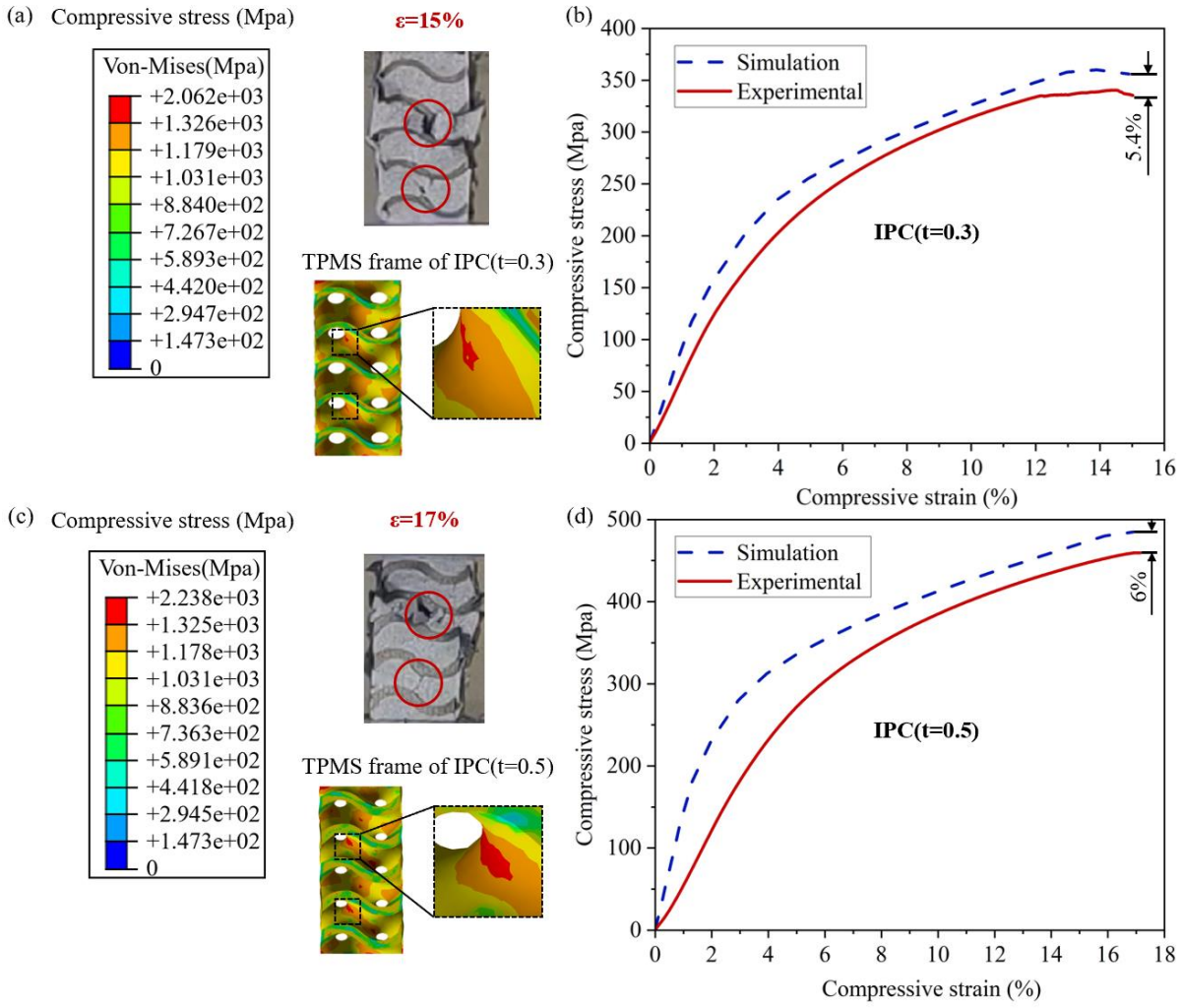

Fig. 7 Comparison between compression tests and numerical simulations at the moment of initial cracking in the TPMS structure of IPC during compression: (a) the location of initial crack in the TPMS structure of IPC (t=0.3) and the simulated cloud image of Von-mises at this strain, (b) experimental and numerical stress-strain curves synchronized to the strains shown in (a), (c) the location of initial crack in the TPMS structure of IPC (t=0.5) and the Von-mises stress at this strain, and (d) experimental and numerical stress-strain curves synchronised to the strains shown in (c).

3.3 Fracture morphology characteristics after compressive testing

The microstructure from fracture surface of the TC4/ZL102 IPCs after compression is shown in Fig. 8. Two fracture surfaces are present, comprising shear and extrusion surfaces. At the shear fracture surface, the ZL102 section exhibits a tear pattern, while the TC4 cross-section is notably smooth shown in Fig. 8d, indicating a cohesive interaction between the two phases with minimal gaps. Upon close inspection at higher magnification, some shallow cracks remain discernible on the smooth TC4 section presented in Fig. 9a. These microscopic cracks converge to form large macroscopic cracks when the fracture surface is under increasing load, indicating that the fracture behaviour of TC4 exhibits some ductility. Small cracks and cleavage facets are evident on the ZL102 surface under high magnification (Fig. 8d and Fig. 9b), demonstrating a tendency toward brittle fracture in ZL102. In the extrusion fracture section, numerous vertical cracks are notably visible in TC4 (Fig. 8e and Fig. 9c), and these cracks are likely to become more pronounced with additional load and compression. The fracture of ZL102 section is composed of many layered cracks and dimples (Fig. 9d). Considering the large shape variable of the IPCs in the experiment, it can be inferred that the fracture form of the specimen is ductile fracture. The predominant fracture mode observed in TC4/ZL102 IPCs is predominantly associated with the interpenetrating TC4 structure.

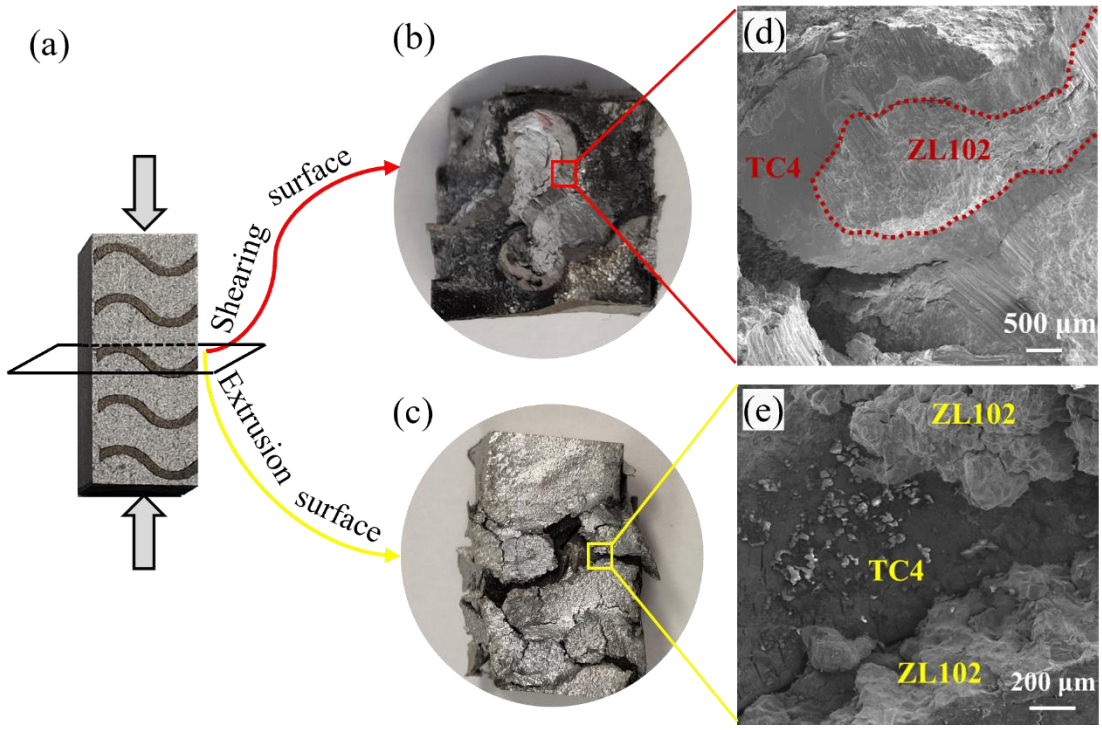

Fig. 8 Microstructure from the fracture surface of TC4/ZL102 IPCs after compression: (a) two kinds of fracture: shear and extrusion fractures, (b) shear fracture cross section, (c) extrusion fracture cross section, (d) a highly magnified image of (b), and (e) a highly magnified image of (c).

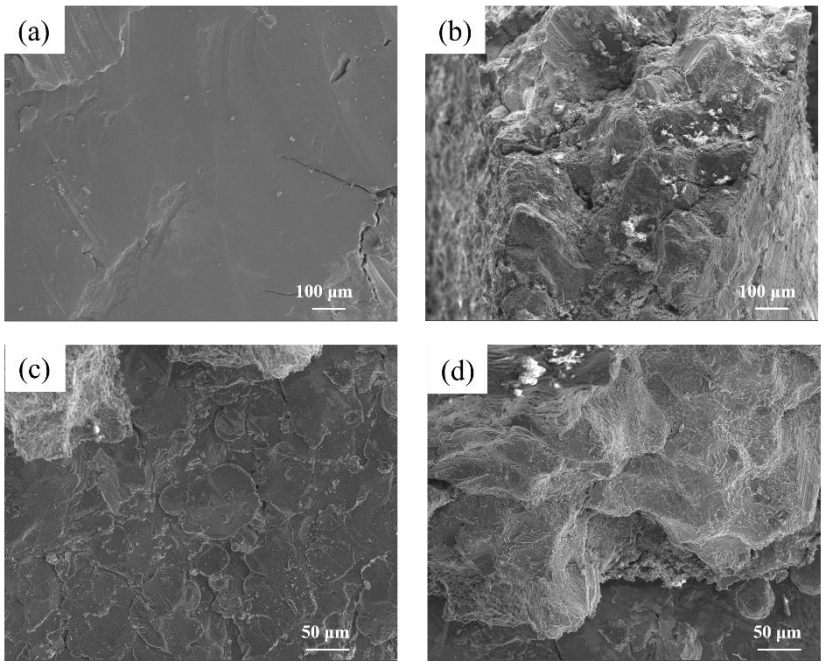

Fig. 9 Microscopic characterisation of the fractured surface of TC4 and ZL102 phases after crushing at a high magnification: (a-b) microstructure of TC4 and ZL102 under the shear fracture, respectively, and (c-d) microstructure of TC4 and ZL102 under the extrusion fracture, respectively.

4 Discussion

4.1 The fracture mechanism in the compression

Ductile fracture of metal involves the nucleation, propagation and merger of voids, leading to the formation of cracks. The formula of the Mohr-Coulomb model has high accuracy in predicting metal fracture. The Mohr-Coulomb model can be described as [61]:

$$\max_{n}[\tau+c_1\sigma_n]=c_\alpha \tag{4}$$

where τ and σ_n represent shear stress and normal stress in the plane of normal vector n, c_1 denotes the friction coefficient and c_α denotes the cohesion coefficient. Specifically, the Mohr-Coulomb model assumes the same pore volume fraction and overlooks the stress state analysis. In contrast, the isotropic Hosford-Coulomb model as proposed by Mohr and Marcadet, proves more effective for metal fracture prediction in this experiment. The ductile metal fracture depends on three principal stresses, and the formula for Hosford-Coulomb model is expressed as [62]:

$$\left\{\frac{1}{2}((\sigma_1-\sigma_2)^a+(\sigma_1-\sigma_3)^a+(\sigma_2-\sigma_3)^a)\right\}^{\frac{1}{a}}+c(\sigma_1+\sigma_3)=\beta \tag{5}$$

where σ_1, σ_2 and σ_3 are the three principal stresses, respectively, a and β denote the Hosford exponent and friction coefficient, respectively. Utilizing the stress analysis methods mentioned earlier, the Cockroft-Latham function is employed to find the cracking place. This facilitates a more convenient identification of the potential for qualitative cracking under the experimental

conditions of quasi-static compression [63], and the function equation is denoted as:

$$\int_0^{\varepsilon_f} \sigma^* \, d\varepsilon = C \tag{6}$$

where σ* denotes the stress, ε_f is a fracture strain, and C is a constant. The ductile fracture is related to the maximum stress height distributed in the pore structure. The cracks of Gyroid structure at the joints of inclined support plates was investigated where the stress was concentrated [44]. The stress concentration of zinc porous structures at the connections of support plates resulted in the cracking process [64]. In order to comprehensively analyse the fracture mechanism and deformation behaviour of the IPCs surface in the compression, a half model is extracted from the IPC unit cell and expanded for structural analysis on a plane, as shown in Fig. 10. A Gyroid unit cell of TC4 TPMS structure comprises four equivalent sub-layers, with two of them forming an "S"-type structure, making the half model sufficient to illustrate the fracture behaviours and stress distribution of the entire structure.

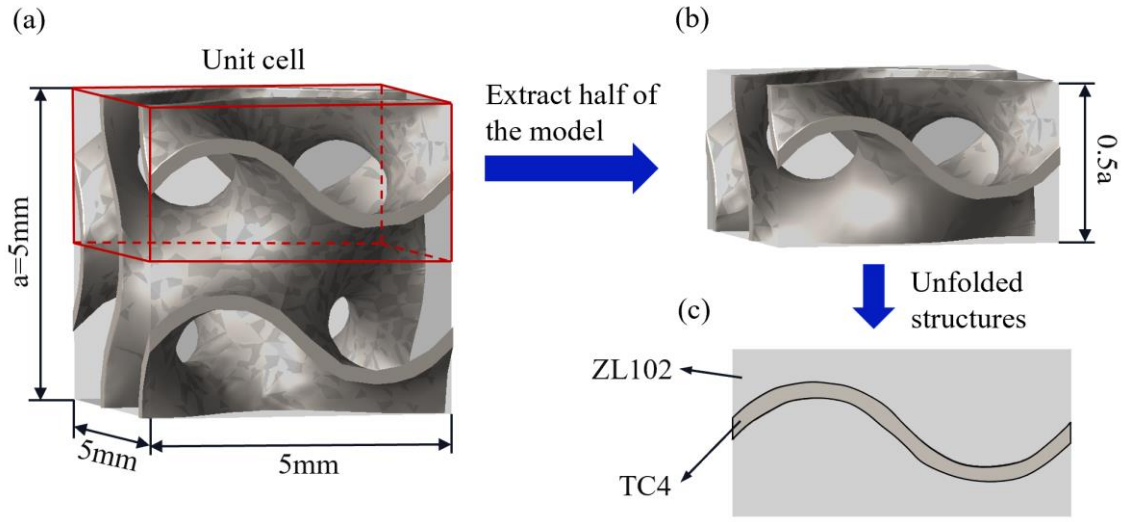

Fig. 10 Schematic diagram of unfolding half IPC unit cell: (a) IPC unit cell, (b) half of the model, and (c) unfolded structure with ZL102 and TC4 structure.

Fig. 11 illustrates a schematic diagram of the free-body IPC structure, depicting the deformation and stress mode of the structure under compressive load. Under compressive load, the filled ZL102 phase produces extrusion stress with the TC4 structure at the two contact surfaces above the left half of the "S" structure and below the right half of the structure. In the compressive loading deformation mode, the contact surface experiencing the primary extrusion pressure establishes a compressive stress zone, while the corresponding opposite side forms a tensile stress zone. These two locations creating a tensile stress zone contribute to the crack propagation of. In this deformation mode, the centerline of the structure exhibits a tendency to stretch, forming a straight line.

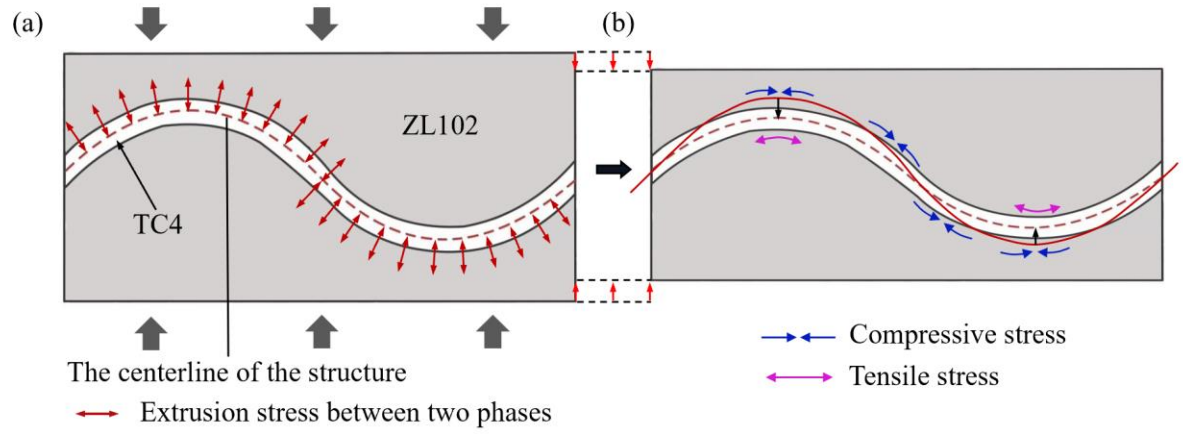

Fig. 11 Schematic diagram of the free-body IPC structure: (a) the initial status, and (b) the deformed status under the compressive loading.

The stress distributions for the TPMS scaffold, TC4 and ZL102 phases of IPC in compression behaviour obtained by the numerical simulation are shown in Fig. 12, respectively. Numerical results reveal that significant stress is concentrated on the helical surface of the structure from top to bottom, and this phenomenon is reflected in both TPMS scaffold and IPC. This verifies that the middle region of the "S" structure has the greatest force under the combined action of tensile and compressive stresses as shown in Fig. 11, and the unfolded two-dimensional region corresponds to the middle part of the formal helical surface of the three-dimensional region. This phenomenon is caused by the Gyroid structure, which rotates the main loading region of the whole specimen, making a more distributed and evenly distributed force. The significant stress concentration region of ZL102 phase is consistent with that of TC4 phase (circled with black in Fig. 12), and the maximum stress value of TC4 phase in IPC is also considerably smaller than that in the individual TPMS scaffold. This stress deviation is roughly consistent with the maximum stress of ZL102 phase in IPC. It indicates that the ZL102 phase can share part of the force under the interpenetrating structure. As expected, the danger zone of maximum stress (circled with red in Fig. 12) emerges as the compression process advances up and down towards the center. This aligns with the region where the initial crack manifested in the actual compressive experiment, as shown in Fig. 13 of next section.

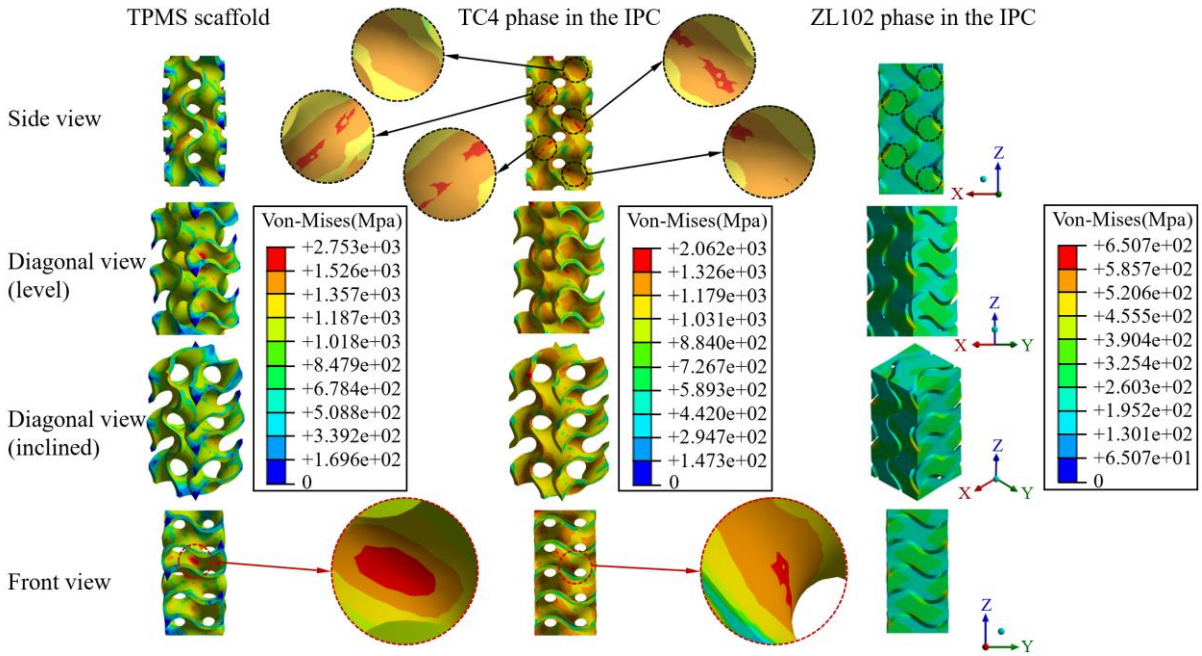

Fig. 12 Von Mises stress distributions of deformed individual TPMS scaffold, and TC4 and ZL102 phases of Ti/Al IPC.

4.2 Effects of porous structure on mechanical properties

To further analyse the deformation behaviour of the two porous IPCs in compression, snapshots of the testing process are shown in Figs. 13a and 13b. Combined with the stress-strain curve characteristics of IPC (Fig. 13c), the damage evolution process of Ti/Al IPC in compression deformation is shown schematically in Fig. 13d. In general, the fracture of IPC can be divided into four stages: initial deformation (Stage 1), the occurrence of micro cracks between two phases (Stage 2), the onset of high-strength alloy deterioration (Stage 3), and the ultimate collapse of the IPC specimen (Stage 4). From the experimental snapshots, it can be observed that small initial cracks appear in the filling ZL102 phase when the strain reaches 5 % for IPC (t=0.3) and 10 % for IPC (t=0.5). This initial crack occurs between the embedded phase and the filling phase, and the initial damage in interpenetrating materials is prone to occur in the form of intergranular cracking between the precipitated and interpenetrating phases [6, 16, 65]. As compression advances, at a strain of 12 % for IPC (t=0.3) and 14 % for IPC (t=0.5), the cracks occur in the interfacial phase, and the ZL102 phase in the pores undergoes extrusion and descends, marking the onset of Stage 3. Moreover, the flow stress of IPC rises during the initial two stages, and the TPMS structure fabricated by the stronger TC4 alloy initiates cracking. This disruption compromises the continuity and integrity of the IPC interpenetrating structure, resulting in a decline in the IPC flow stress in Stage 3. This phenomenon is highly consistent with the numerical results where the TPMS structure starts to show a large stress concentration

region at 15 % and 17 % strain for IPC (t=0.3) and IPC (t=0.5), respectively, shown in Fig.7. The TPMS structure forms microcracks at locations such as air holes, incompletely sintered powder inclusions and areas of insufficient sintering between adjacent layers. These defects are not fully understood in terms of their formation mechanisms and appear to be unavoidable in 3D printed metals [66, 67]. Subsequently, cracks expand and merge until the strain reaches 34% for IPC (t=0.3) and 24% for IPC (t=0.5). The cracks in the TPMS frame merge, join, and expand, forming slip bands. This process is accompanied by a large amount of plastic deformation and slip of ZL102, resulting in a steep drop of the IPC flow stress, indicating the IPC failure. The thicker TPMS structure of IPC(t=0.5) results in a higher value of Young's modulus, causing a faster rise in the stress-strain curve during Stages 1 and 2. The progression of Stage 4 determines the maximum strain limit at the collapse of IPC. The greater work-hardening coefficient of IPC (t=0.3) results in a more evenly distributed compressive deformation, extending the compression of stress-strain curve for a longer duration from Stage 3 to Stage 4.

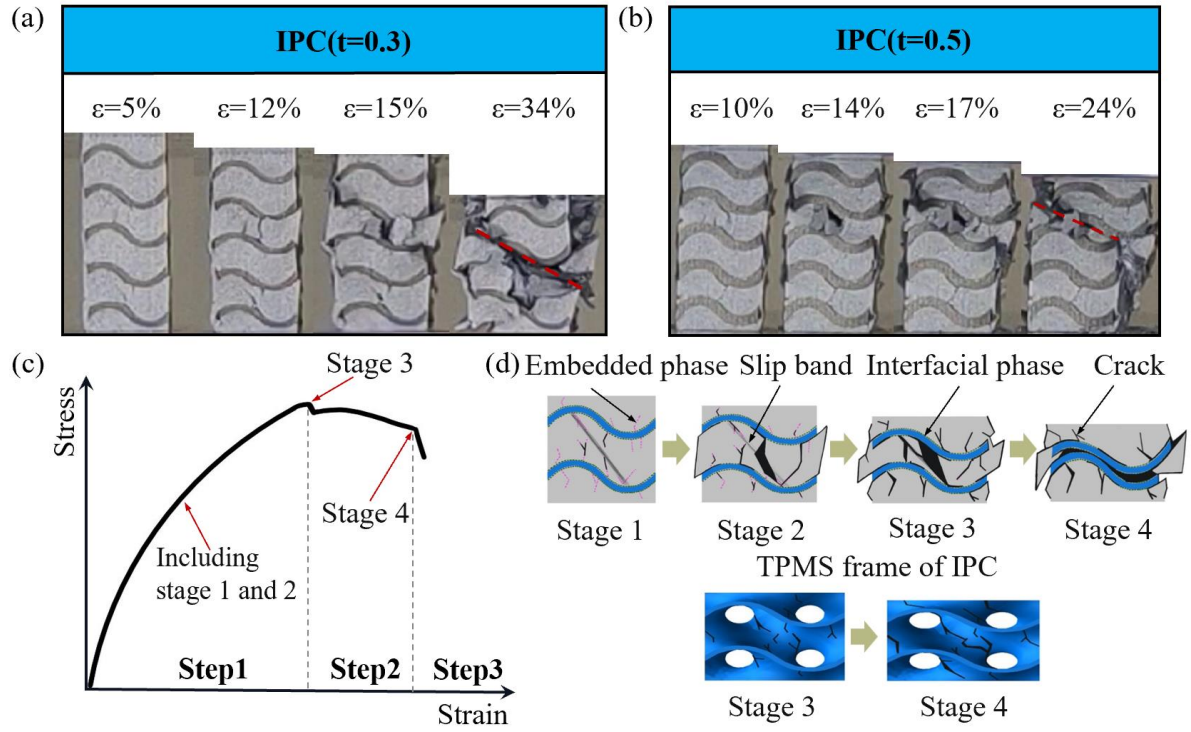

Fig. 13 Compressive behavior of two porous IPC samples at different strain rates: (a) IPC (t=0.3) and (b) IPC (t=0.5), (c) stress-strain curve of Ti/Al IPC, and (d) schematic representation of the IPC damage evolution process during the compressive deformation.

4.3 Comparison of mechanical properties

The comparison of strength and energy absorption efficiency in terms of maximum transmitted stress for Ti/Al IPCs and other materials was conducted to demonstrate the excellent

mechanical properties of the fabricated Ti/Al IPCs, as shown in Fig. 14. It is noted that the maximum transmitted stress and the energy absorption efficiency are two basic parameters for evaluating the energy absorption performance of a material, which are defined by the peak stress and the area under the stress-strain curve, respectively. It can be seen that our fabricated Ti/Al IPC outperforms most Al alloys, metals, micro lattice and polymer foams and other commonly used energy absorbing materials in terms of the combination of energy absorption efficiency and load carrying capacity. Specifically, in both structural frames with different porosities, the Ti/Al IPC exhibits a period of slowly declining plateau from Stage 3 to Stage 4 of the stress-strain curve, which provides the basis for enhanced energy absorption. In general, stress-strain curves for dense metals exhibit a continuous rise, which is not favourable for energy absorption since the stress applied during energy absorption usually falls below the yield strength of the material. This results in high energy absorption efficiencies for Ti/Al IPCs, exceeding the general range for Ti, Al and alloys, and comparable to those for steel. Additionally, the comparison of properties for the Ti/Al IPCs and a number of other proposed IPCs was conducted [6, 20, 60, 65], and several of them have high energy absorption efficiencies at comparable load-bearing capacities due to their selection of higher-strength metals for interpenetration. However, it is worth mentioning that Ti/Al IPCs achieve equivalent load-bearing capacity on the basis of simpler interpenetration, lighter material properties and greater economy.

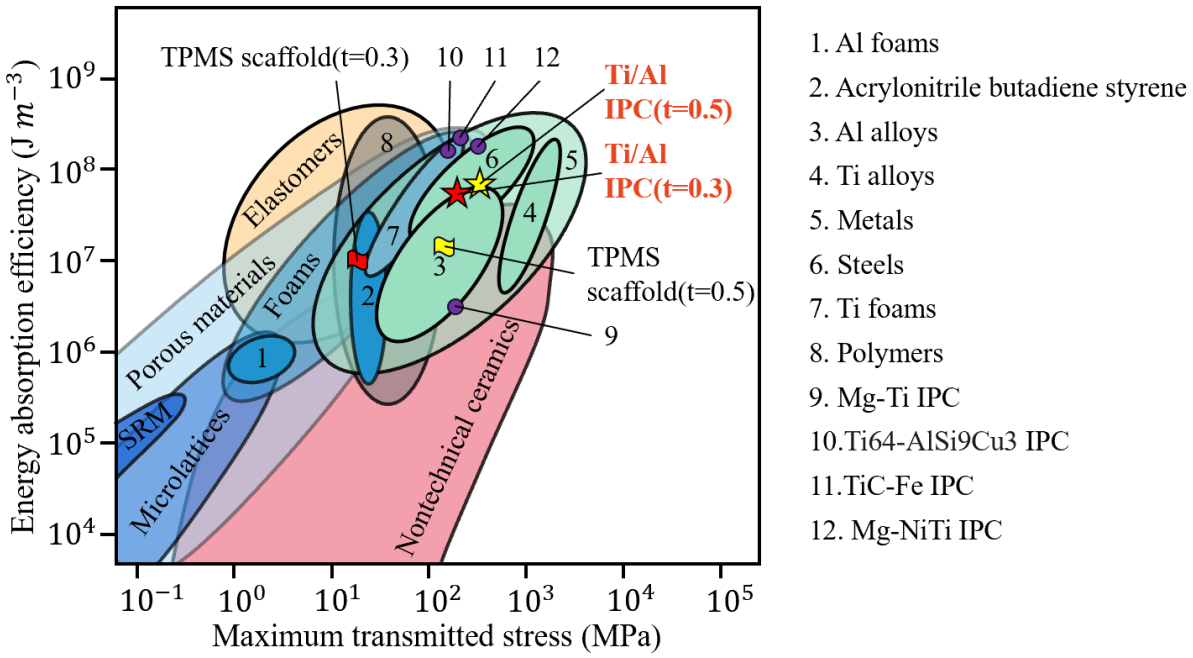

Fig. 14 Comparison of Ti/Al IPC properties with other materials: energy absorption per unit volume versus maximum transmitted stress for IPCs, titanium alloys and a wide range of other materials, particularly those commonly used for energy absorption.

5 Conclusions

The characteristics of microstructure, mechanical properties and fracture behaviours for Ti/Al IPCs in compression testing were investigate in this study. The main conclusions of this research are obtained as follows:

1. The Young's modulus, yield stress and maximum compressive stress of the IPCs are notably superior to those of individual additive-manufactured TPMS scaffolds. The interpenetrating structure improves the compressive property and strength of the multi-metamaterial, and the enhancement of the compressive stress limit. The numerical results are consistent with the experimental results, the initial cracks of the framework appear in the middle of the samples, leading to the decrease of the stress-strain curve of the IPC.
2. The TPMS structure of IPC (t=0.5) is more substantial, exhibiting a higher Young's modulus, and the stress-strain curve rises more rapidly during the initial deformation stage. The prolonged destruction of the TPMS structure determines the maximum strain limit at IPC collapse. The increased work-hardening coefficient of IPC (t=0.3) results in a more homogeneous degree of compressive deformation, causing the stress-strain curve to compress for an extended duration at this stage.
3. The central symmetrical tensile and compressive stress zones appear in the "S" structure of Ti/Al IPCs, causing the composite structure to incline toward a straight alignment. The region corresponding to stress concentration is the central region of the helical surface, and the region of maximum stress concentration is consistent between ZL102 phase and TC4 phase, with the ZL102 phase effectively redistribution and sharing a portion of the loading.
4. The IPCs as a whole exhibit a ductile metal fracture mode, and the fracture mode of TC4 is malleable. The fracture of TC4 phase bearing the majority of the loading is the main reason for the failure of Ti/Al IPCs. The interrupted spaces at the interpenetrated interface of the Ti/Al IPC hinder the efficient transfer of loads from the TC4 phase to the ZL102 phase during compression, leading to slippage in the compression of the ZL102 phase.
5. Ti/Al IPCs surpasses conventional energy-absorbing materials, showcasing superior energy absorption efficiency and load-bearing capacity. This exceptional performance exceeds typical ranges for Ti, Al, and alloys, rivaling that of steel. Comparisons with other proposed IPCs underscore the Ti/Al IPC's economic advantage, achieving equivalent load-bearing capacity through simpler interpenetration and lighter materials.

Declaration of competing interest

There is no conflict of interest.

Acknowledgments

The authors wish to gratefully acknowledge the financial support from the National Natural Science Foundation of China (Grant No. 52105418), the Natural Science Foundation of Hunan Province (Grant No. 2023JJ20069), and the key scientific research project of Hunan Provincial Department of Education (Grant No. 23A0001).

References

1. Yang, X., et al., *Functional application of multi-element metal composite materials.* Journal of Alloys and Compounds, 2022. **895**: p. 162622.
2. Li, Z., et al., *The Plastic Deformation Mechanism in Nano-Polycrystalline Al/Mg Layered Composites: A Molecular Dynamics Study.* 2024. **14**.
3. Lin, F., et al., *Achieving balanced strength-ductility of heterostructured TiC/graphene nanoplatelets (GNPs) reinforced Al matrix composites by tuning TiC-to-GNPs ratio.* Composites Communications, 2023. **38**: p. 101529.
4. Lin, F., et al., *Effects of TiB2 content on microstructural evolution, microhardness and tribological behaviours of Al matrix composites reinforced with TiB2 particles.* Ceramics International, 2024.
5. Singh, A., O. Al-Ketan, and N. Karathanasopoulos, *Mechanical performance of solid and sheet network-based stochastic interpenetrating phase composite materials.* Composites Part B: Engineering, 2023. **251**: p. 110478.
6. Zhang, M., et al., *On the damage tolerance of 3-D printed Mg-Ti interpenetrating-phase composites with bioinspired architectures.* Nature Communications, 2022. **13**(1): p. 3247.
7. Feng, X.Q., et al., *Effective elastic and plastic properties of interpenetrating multiphase composites.* Applied Composite Materials, 2004. **11**(1): p. 33-55.
8. Ai, L. and X.L. Gao, *Evaluation of effective elastic properties of 3D printable interpenetrating phase composites using the meshfree radial point interpolation method.* Mechanics of Advanced Materials and Structures, 2018. **25**(15-16): p. 1241-1251.
9. Viet, N.V., et al., *Effective compressive behavior of functionally graded TPMS titanium implants with ingrown cortical or trabecular bone.* Composite Structures, 2023. **303**.
10. Kouzeli, M. and D.C. Dunand, *Effect of reinforcement connectivity on the elasto-plastic behavior of aluminum composites containing sub-micron alumina particles.* Acta Materialia, 2003. **51**(20): p. 6105-6121.
11. Okulov, I.V., et al., *Anomalously low modulus of the interpenetrating-phase composite of Fe and Mg obtained by liquid metal dealloying.* Scripta Materialia, 2019. **163**: p. 133-136.
12. Zhang, C., et al., *The wrinkling and buckling of graphene induced by nanotwinned copper matrix: A molecular dynamics study.* Nano Materials Science, 2021. **3**(1): p. 95-103.
13. Zhang, W., X. Xue, and H. Bai, *Mechanical and electrical properties of Cu-Steel bimetallic porous composite with a double-helix entangled structure.* Composite Structures, 2021. **255**: p. 112886.
14. Zhu, J., et al., *Interfacial structure and stability of a co-continuous SiC/Al composite prepared by vacuum-pressure infiltration.* Ceramics International, 2017. **43**(8): p. 6563-6570.
15. Yang, J., et al., *Interpenetrating phase composite graded lattice structure integrated with load-bearing and sensing capabilities.* Composites Part A: Applied Science and Manufacturing, 2023. **164**: p. 107294.
16. Holovenko, Y., et al., *Effect of lattice surface treatment on performance of hardmetal - titanium interpenetrating phase composites.* International Journal of Refractory Metals and Hard Materials, 2020. **86**: p. 105087.
17. Okulov, I.V., et al., *Anomalous compliance of interpenetrating-phase composite of Ti and Mg synthesized by liquid metal dealloying.* Scripta Materialia, 2021. **194**: p. 113660.
18. Zheng, Y., et al., *Synthesis and mechanical properties of TiC-Fe interpenetrating phase composites fabricated by infiltration process.* Ceramics International, 2018. **44**(17): p. 21742-21749.
19. Li, Z., et al., *A novel Ti/Al interpenetrating phase composite with enhanced mechanical properties.* Materials Letters, 2024. **357**: p. 135723.

20. Lei, J., et al., *Interfacial microstructure evolution for coordinated deformation of Mg/Al composite plates by asymmetrical rolling with differential temperature rolls.* Journal of Magnesium and Alloys, 2023.
21. Wang, X., et al., *3D printing of polymer matrix composites: A review and prospective.* Composites Part B: Engineering, 2017. **110**: p. 442-458.
22. Zhang, L., et al., *3D direct printing of mechanical and biocompatible hydrogel meta-structures.* Bioactive Materials, 2022. **10**: p. 48-55.
23. Zhou, X., et al., *3D Printed scaffolds with hierarchical biomimetic structure for osteochondral regeneration.* Nanomedicine: Nanotechnology, Biology and Medicine, 2019. **19**: p. 58-70.
24. Belhabib, S. and S. Guessasma, *Compression performance of hollow structures: From topology optimisation to design 3D printing.* International Journal of Mechanical Sciences, 2017. **133**: p. 728-739.
25. Zhong, L., et al., *3D printing of hollow fiber nanothermites with cavity-mediated self-accelerating combustion.* Journal of Applied Physics, 2021. **129**(10).
26. Li, W., et al., *3D printing of heterogeneous microfibers with multi-hollow structure via microfluidic spinning.* Journal of Tissue Engineering and Regenerative Medicine, 2022. **16**(10): p. 913-922.
27. Nguyen, T.H.M., et al., *Porous structures prepared by a novel route: Combination of digital light processing 3D printing and leaching method.* Journal of Manufacturing Processes, 2021. **67**: p. 46-51.
28. Wang, B., L.J. Sun, and B. Pan, *Mapping internal deformation fields in 3D printed porous structure with digital volume correlation.* Polymer Testing, 2019. **78**.
29. Men, N.T.H., et al., *Porous structures prepared by a novel route: Combination of digital light processing 3D printing and leaching method.* Journal of Manufacturing Processes, 2021. **67**: p. 46-51.
30. Lei, Y., et al., *A scale-elastic discrete grid structure for voxel-based modeling and management of 3D data.* International Journal of Applied Earth Observation and Geoinformation, 2022. **113**: p. 103009.
31. Lu, C., et al., *Mechanical Performance of 3D-Printing Plastic Honeycomb Sandwich Structure.* International Journal of Precision Engineering and Manufacturing-Green Technology, 2018. **5**(1): p. 47-54.
32. Ye, Y.Q., et al., *The effects of grid design on the performance of 3D-printed dry powder inhalers.* International Journal of Pharmaceutics, 2022. **627**.
33. Li, K., et al., *A domain adversarial graph convolutional network for intelligent monitoring of tool wear in machine tools.* Computers & Industrial Engineering, 2024. **187**: p. 109795.
34. Kanwar, S. and S. Vijayavenkataraman, *3D printable bone-mimicking functionally gradient stochastic scaffolds for tissue engineering and bone implant applications.* Materials & Design, 2022. **223**: p. 111199.
35. Wang, Y., et al., *Three-dimensional metal printing injection mold gradient space structure is manufactured by performing injection mold designing according to injection characteristic, and manufacturing injection mold through metal printing mode*. Univ Xian Jiaotong (Uyxj-C) Univ Xian Jiaotong (Uyxj-C).
36. Zeng, Y., et al., *Fabrication of alumina ceramics with functional gradient structures by digital light processing 3D printing technology.* Ceramics International, 2022. **48**(8): p. 10613-10619.
37. Ahmadi, M., et al., *Review of selective laser melting of magnesium alloys: advantages, microstructure and mechanical characterizations, defects, challenges, and applications.* Journal of Materials Research and Technology, 2022. **19**: p. 1537-1562.
38. Sefene, E.M., *State-of-the-art of selective laser melting process: A comprehensive review.* Journal of Manufacturing Systems, 2022. **63**: p. 250-274.
39. Liang, B., D. Zhou, and X. Han, *Selective laser sintering of phase change composites for thermal management systems.* Materials Today: Proceedings, 2022. **70**: p. 248-251.

40. Grossin, D., et al., *A review of additive manufacturing of ceramics by powder bed selective laser processing (sintering / melting): Calcium phosphate, silicon carbide, zirconia, alumina, and their composites.* Open Ceramics, 2021. **5**: p. 100073.
41. Lin, Z., S. Dadbakhsh, and A. Rashid, *Developing processing windows for powder pre-heating in electron beam melting.* Journal of Manufacturing Processes, 2022. **83**: p. 180-191.
42. Uçak, N., A. Çiçek, and K. Aslantas, *Machinability of 3D printed metallic materials fabricated by selective laser melting and electron beam melting: A review.* Journal of Manufacturing Processes, 2022. **80**: p. 414-457.
43. Guest, J.K. and J.H. Prévost, *Optimizing multifunctional materials: Design of microstructures for maximized stiffness and fluid permeability.* International Journal of Solids and Structures, 2006. **43**(22): p. 7028-7047.
44. Yang, L., et al., *Compression–compression fatigue behaviour of gyroid-type triply periodic minimal surface porous structures fabricated by selective laser melting.* Acta Materialia, 2019. **181**: p. 49-66.
45. Gao, T., et al., *Elastic mechanical property hybridization of configuration-varying TPMS with geometric continuity.* Materials & Design, 2022. **221**: p. 110995.
46. Yan, C., et al., *Advanced lightweight 316L stainless steel cellular lattice structures fabricated via selective laser melting.* Materials & Design, 2014. **55**: p. 533-541.
47. Gandy, P.J.F., et al., *Exact computation of the triply periodic D (`diamond') minimal surface.* Chemical Physics Letters, 1999. **314**(5): p. 543-551.
48. Gandy, P.J.F. and J. Klinowski, *Exact computation of the triply periodic G (`Gyroid') minimal surface.* Chemical Physics Letters, 2000. **321**(5): p. 363-371.
49. Tang, W., et al., *Analysis on the convective heat transfer process and performance evaluation of Triply Periodic Minimal Surface (TPMS) based on Diamond, Gyroid and Iwp.* International Journal of Heat and Mass Transfer, 2023. **201**: p. 123642.
50. Cai, J., Y. Ma, and Z. Deng, *On the effective elastic modulus of the ribbed structure based on Schwarz Primitive triply periodic minimal surface.* Thin-Walled Structures, 2022. **170**: p. 108642.
51. Bonatti, C. and D. Mohr, *Smooth-shell metamaterials of cubic symmetry: Anisotropic elasticity, yield strength and specific energy absorption.* Acta Materialia, 2019. **164**: p. 301-321.
52. Jia, H., et al., *An experimental and numerical investigation of compressive response of designed Schwarz Primitive triply periodic minimal surface with non-uniform shell thickness.* Extreme Mechanics Letters, 2020. **37**: p. 100671.
53. Novak, N., et al., *Quasi-static and dynamic compressive behaviour of sheet TPMS cellular structures.* Composite Structures, 2021. **266**: p. 113801.
54. Qureshi, Z.A., et al., *On the effect of porosity and functional grading of 3D printable triply periodic minimal surface (TPMS) based architected lattices embedded with a phase change material.* International Journal of Heat and Mass Transfer, 2022. **183**: p. 122111.
55. Sreedhar, N., et al., *Mass transfer analysis of ultrafiltration using spacers based on triply periodic minimal surfaces: Effects of spacer design, directionality and voidage.* Journal of Membrane Science, 2018. **561**: p. 89-98.
56. Wallat, L., et al., *Energy absorption capability of graded and non-graded sheet-based gyroid structures fabricated by microcast processing.* Journal of Materials Research and Technology, 2022. **21**: p. 1798-1810.
57. Zhou, Z., et al., *Ultra-fine Nbss/Nb5Si3 in situ composites with remarkable properties prepared by ultrasonic melt treatment.* Journal of Alloys and Compounds, 2023. **940**: p. 168940.

58. Wang, X.J., et al., *Processing, microstructure and mechanical properties of micro-SiC particles reinforced magnesium matrix composites fabricated by stir casting assisted by ultrasonic treatment processing.* Materials & Design, 2014. **57**: p. 638-645.
59. Sun, Q., et al., *Compressive mechanical properties and energy absorption characteristics of SLM fabricated Ti6Al4V triply periodic minimal surface cellular structures.* Mechanics of Materials, 2022. **166**: p. 104241.
60. Tulpan, I., et al., *Effect of the lattice structure on the interface zone and the final properties of novel PrintCast Ti64-AlSi9Cu3 interpenetrating phase composites.* Additive Manufacturing, 2024. **79**: p. 103902.
61. Dunand, M. and D. Mohr, *On the predictive capabilities of the shear modified Gurson and the modified Mohr–Coulomb fracture models over a wide range of stress triaxialities and Lode angles.* Journal of the Mechanics and Physics of Solids, 2011. **59**(7): p. 1374-1394.
62. Mohr, D. and S.J. Marcadet, *Micromechanically-motivated phenomenological Hosford–Coulomb model for predicting ductile fracture initiation at low stress triaxialities.* International Journal of Solids and Structures, 2015. **67-68**: p. 40-55.
63. Cockcroft, M.G. and D.J. Latham, *Ductility and the Workability of Metals.* Journal Institute of Metals, 1968. **96**: p. 33-39.
64. Li, Y., et al., *Corrosion fatigue behavior of additively manufactured biodegradable porous zinc.* Acta Biomaterialia, 2020. **106**: p. 439-449.
65. Zhang, M., et al., *3D printed Mg-NiTi interpenetrating-phase composites with high strength, damping capacity, and energy absorption efficiency.* Science Advances, 2020. **6**(19): p. eaba5581.
66. Vyatskikh, A., et al., *Additive manufacturing of 3D nano-architected metals.* Nature Communications, 2018. **9**(1): p. 593.
67. Hu, G., et al., *Ultrasonic-assisted direct writing metal additive manufacturing technique.* Journal of Materials Processing Technology, 2023. **312**: p. 117830.

https://dspace.org/

Compressive properties and fracture behaviours of Ti/Al interpenetrating phase composites with additive-manufactured triply periodic minimal surface porous structures

Li, Zhou; Mo, Haotian; Tian, Jiahao; Li, Junhao; Xia, Shiqi ...

2025-04
Springer
https://doi.org/10.1007/s12540-024-01797-4
Li Z, Mo H, Tian J, et al., (2025) Compressive properties and fracture behaviours of Ti/Al interpenetrating phase composites with additive-manufactured triply periodic minimal surface porous structures. Metals and Materials International, Volume 31, Issue 4, April 2025, pp. 955-970

Downloaded from a DSpace repository. https://dspace.org/